J. Fluid Mech. (2004), *vol.* 514, *pp.* 153–172.
DOI: 10.1017/S0022112004000035 Printed in the United Kingdom

Direct numerical simulation and large-eddy simulation of a shear-free mixing layer

By B. KNAEPEN[1], O. DEBLIQUY[2] AND D. CARATI[2]

[1]Center for Turbulence Research, Stanford University/NASA Ames Research Center, 488 Escondido Mall, Building 500/500A, Stanford University, CA 94305-3035, USA

[2]Universté Libre de Bruxelles, Statistical and Plasma Physics, CP231, Boulevard du Triomphe, Campus Plaine, 1050 Brussels, Belgium

(Received 29 April 2003 and in revised form 13 April 2004)

High resolution direct numerical simulation (DNS) ($512 \times 1024 \times 512$) and large-eddy simulation (LES) of a shear-free mixing layer are presented. The geometry of the flow consists of two layers with different turbulence intensities that are in contact and interact through a fairly thin mixing layer. This geometry is used to explore the influence of inhomogeneities in the characteristic length scales, times scales and energy scales on the turbulence properties. Comparison of DNS results is made with the Veeravalli & Warhaft (*J. Fluid Mech.* **207**, 191–229, 1989) experiment. The LES is performed on a $32 \times 64 \times 32$ grid using an eddy-viscosity model. The use of such a model appears to be justified by the very weak departures from isotropy that are observed in the shear-free mixing layer. The LES predictions are compared with the filtered DNS data and show that the eddy viscosity model performs very well in predicting the energy profile as well as the deviation from Gaussianity in the turbulent velocity field statistics.

1. Introduction

The shear-free mixing layer represents one of the simplest inhomogeneous flows. It consists of two 'distinct' homogeneous regions of different turbulent kinetic energy interacting through a layer of rapid transition. The layer is said to be shear-free since the two homogeneous regions have no relative velocity. While flows encountered in nature or industrial applications are more often not devoid of shear, the study of the shear-free mixing layer is nevertheless useful since it allows the mixing properties of turbulence to be examined in a simplified environment. Indeed, turbulent transport properties in shear flows are more difficult to track since they can be overwhelmed by production sources originating from gradients in the mean velocity.

The shear-free mixing layer has already received attention in the past, both from the experimental and the numerical point of view. The first experimental study of the shear-free mixing layer is due to Gilbert (1980). The flow was obtained by forcing a stream through a grid with two different mesh spacings. The two sides of the grid have, however, equal solidity resulting in an outgoing shear-free flow. In this first experimental study, Gilbert mainly concentrated his attention on the downstream evolution of the spreading-rate parameter, which is a measure of the thickness of the mixing-layer. A more extensive experimental study was later performed by Veeravalli & Warhaft (1987, 1989). Owing to a different experimental set-up, they achieved a higher ratio between the energies characterizing the two sides of the flow

and this resulted in the observation of large-scale intermittency in the flow. The Veeravalli & Warhaft (1989) data will be used here as the main benchmark for the present study since they contain a detailed documentation of the flow characteristics we will be examining. From the numerical point of view, the shear-free mixing layer was studied in Briggs *et al.* (1996) using direct numerical simulation (DNS). In that article, the authors also used the data of Veeravalli & Warhaft (1989) as the point of comparison. Their simulations used a spectral code with a resolution of 128^3 Fourier modes. The microscale Reynolds numbers reached in the low- and high-energy homogeneous regions were, respectively, 11 and 22.5, which are roughly half of the values reported in the Veeravalli & Warhaft (1989) experiment (note that Briggs *et al.* (1996) use a different definition of the microscale Reynolds number from that in Veeravalli & Warhaft (1989) and here). However, when properly non-dimensionalized, they were able to reproduce satisfactorily the turbulence statistics of the flow.

The purpose of this work is twofold. First, given the computational resources available today, it is possible to reach, using DNS, higher Reynolds numbers than in Briggs *et al.* (1996). In the present study, the microscale Reynolds numbers reached in the low- and high-energy homogeneous regions are, respectively, 32 and 69. The results reported earlier can thus be complemented and their robustness in the presence of increased turbulence studied. The second aim of this work is to perform a detailed and documented large-eddy simulation (LES) of the shear-free mixing layer. In that respect, the creation of a DNS database at higher Reynolds number is necessary in order to make meaningful LES assessments. The shear-free mixing-layer allows us to test how traditional LES models perform in the presence of an inhomogeneity without having to deal with difficult numerical issues. Indeed, as argued in Briggs *et al.* (1996), it is possible to use a spectral code to study the shear-free mixing layer and we can thus focus on the accuracy of the modelling while avoiding contamination of the results by commutation errors, etc.

This paper is organized as follows. First, we detail the initialization procedure used in the simulation. Since the flow is not statistically stationary, this initialization procedure has a fairly strong influence on the evolution. Although we will focus here on the shear-free mixing layer, the method proposed in the present work can easily be used for other flows with one inhomogeneous direction. The next section of the article is devoted to the description of the DNS. All the relevant parameters are listed and comparison is made with the Veeravalli & Warhaft (1989) experiment. In particular, measurements of inhomogeneity, anisotropy, deviations from Gaussianity and kinetic energy balance are presented. The section on the LES of the shear-free mixing layer follows. A detailed comparison between the filtered DNS data and the LES predictions is presented. It is shown that simple eddy-viscosity models perform very well for the present test case, most probably because the flow seems to be almost isotropic in the small-scale range that is not resolved by the LES.

2. Initialization of the flow

From the numerical point of view, one of the most appealing properties of the shear-free mixing layer is the possibility of simulating this flow with a purely spectral three-dimensional code. Indeed, periodicity can be enforced by considering a second mixing-layer, which performs the 'reverse' transition compared to the first one. The situation is depicted in figure 1. This also has the advantage that results gathered from the two mixing layers can be averaged to improve the statistics. This possibility will

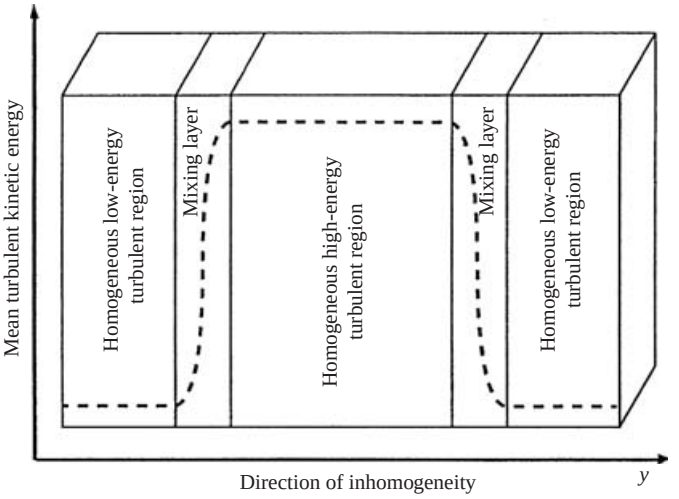

FIGURE 1. Graphical representation of the shear-free mixing layer.

be systematically exploited in the presentation of numerical results in the following sections.

Given a three-dimensional spectral code, the non-trivial part of the simulation is then to build a suitable initial condition that mimics the mixing layer. Indeed, because the decaying mixing layer is not statistically stationary, it is not acceptable to wait until the initial condition is forgotten by the flow due to the stochastic nature of turbulence. Indeed, the simulation will remain quite strongly influenced by the initial state of the velocity field. To proceed, it is necessary to introduce a few definitions and notations. The Fourier modes associated with the velocity field $u_i(x, y, z)$ will be denoted $\tilde{u}_i(k_x, k_y, k_z)$ and are defined by

$$\tilde{u}_i(k_x, k_y, k_z) = \sum_{\boldsymbol{x}} u_i(x, y, z)\mathrm{e}^{-\mathrm{i}\boldsymbol{k}\cdot\boldsymbol{x}}. \tag{2.1}$$

Since the mixing layer is homogeneous in two directions, it is also convenient to consider two-dimensional Fourier transforms. Here, we take the y-direction as the inhomogeneous direction and define the two-dimensional Fourier modes $\tilde{u}_i(k_x, y, k_z)$ by

$$\tilde{u}_i(k_x, y, k_z) = \sum_{\boldsymbol{x}_\perp} u_i(x, y, z)\exp(-\mathrm{i}\boldsymbol{k}_\perp\cdot\boldsymbol{x}_\perp), \tag{2.2}$$

where $\boldsymbol{x}_\perp = (x, z)$ and $\boldsymbol{k}_\perp = (k_x, k_z)$. For convenience, we will also adopt the following notations: $u_x \equiv u$, $u_y \equiv v$ and $u_z \equiv w$. When the flow is homogeneous and isotropic, a common way to initialize the modes $\tilde{u}_i(k_x, k_y, k_z)$ is to fix their amplitudes to match a given energy spectra $E(k)$ and assign them random phases in such a way that continuity is enforced (see e.g. Rogallo 1981). One then has,

$$\langle|\tilde{u}_i(k_x, k_y, k_z)|^2\rangle = A^2(k) \quad \text{with } E(k) = 2\pi k^2 A^2(k), \tag{2.3}$$

and $k^2 = k_x^2 + k_y^2 + k_z^2$. For the case at hand, we can adopt a similar strategy but consider instead the two-dimensional spectra in each plane perpendicular to the direction of inhomogeneity. Indeed, in those planes the flow is assumed to be homogeneous and isotropic. We thus initialize our flow by imposing the following constraints on the two-dimensional Fourier modes (the assignment of the random phases and the treatment of continuity will be described below),

$$\langle|\tilde{u}_i(k_x, y, k_z)|^2\rangle = B^2(k_\perp, y) \quad \text{with } E(k_\perp, y) = \pi k_\perp B^2(k_\perp, y), \tag{2.4}$$

and $k_\perp^2 = k_x^2 + k_z^2$. In (2.4), $E(k_\perp, y)$ is the energy spectra of the velocity field in the (x, z)-plane. The arbitrary part remaining is the choice of the function $B^2(k_\perp, y)$. For homogeneous isotropic flows, it is trivial to relate the two-dimensional amplitudes to the three-dimensional amplitudes (using Parseval's theorem):

$$B^2(k_\perp, y) = \int \mathrm{d}k_y A^2\left(k_y^2 + k_\perp^2\right). \tag{2.5}$$

Note that, as expected, $B^2(k_\perp, y)$ is independent of y for homogeneous flows. In the case of the shear-free mixing layer, we will choose an amplitude function $A(k)$ for each homogeneous region and compute the corresponding functions $B(k_\perp, y)$ using (2.5). If the two-dimensional amplitude functions in the high-energy and low-energy regions are, respectively, denoted $B_H(k_\perp, y)$ and $B_L(k_\perp, y)$, we then define the complete two-dimensional amplitude function for the shear-free mixing layer as,

$$B_{ML}(k_\perp, y) = (1 - f(y))B_L(k_\perp, y) + f(y)B_H(k_\perp, y). \tag{2.6}$$

The function $f(y)$ is equal to 0 in the low-energy region and equal to 1 in the high-energy region; inside the mixing layers, it varies smoothly from 0 to 1. The complete initialization procedure is as follows. First, we initialize our three-dimensional Fourier modes using the procedure of Rogallo (1981). The three-dimensional energy spectra used here is taken from the high-energy homogeneous region of the mixing layer. This ensures that the Fourier modes $\tilde{u}_i(k_x, k_y, k_z)$ satisfy the continuity equation. The three-dimensional Fourier modes are then transformed to $\tilde{u}_i(k_x, y, k_z)$ using a one-dimensional Fourier transform. At this point, their two-dimensional amplitudes are measured and the modes are rescaled in order to match the prescribed two-dimensional amplitudes given by (2.6):

$$\tilde{u}_i(k_x, y, k_z) \to \tilde{u}_i'(k_x, y, k_z) = \tilde{u}_i(k_x, y, k_z)\sqrt{\frac{B_{ML}(k_\perp, y)}{|\tilde{u}_i(k_x, y, k_z)|^2}}. \tag{2.7}$$

The $\tilde{u}_i'(k_x, y, k_z)$ are then transformed back into three-dimensional Fourier modes, $\tilde{u}_i'(k_x, k_y, k_z)$. By performing the transformation (2.7), we, of course, destroy the continuity property of the initial field and it has to be recovered by projecting the $\tilde{u}_i'(k_x, k_y, k_z)$ onto a divergence-free field:

$$\tilde{u}_i'(k_x, k_y, k_z) \to \tilde{u}_i''(k_x, k_y, k_z) = \left(\delta_{ij} - \frac{k_i k_j}{k^2}\right)\tilde{u}_j'(k_x, k_y, k_z). \tag{2.8}$$

This, in turn, partly undoes the prescription of the two-dimensional amplitudes. Fortunately, by iterating the transformations (2.7) and (2.8), we converge to a velocity field that has two-dimensional amplitudes arbitrarily close to $B_{ML}(k_\perp, y)$ and which satisfies continuity. At this stage, the flow still has random phases. In order to correct this problem, we have time evolved the flow until the global skewness of the velocity derivatives reached a converged value. Between each time step, the mixing layer was rebuilt using (2.7) and (2.8) in order to retain the desired two-dimensional amplitudes profile. After that, we stopped the rebuilding procedure and let the flow decay freely.

3. DNS results

3.1. *Parameters of the simulation*

The choice of parameters for the DNS was mainly guided by the following considerations. In order to have an experimental reference to compare with, the

parameters of the DNS have been chosen to match as closely as possible those from the Veeravalli & Warhaft (1989) experiment performed using the 3 : 1 perforated plate. Of course, since numerical capabilities are not unlimited, some compromises had to be made. The most important restriction in the present study is the ability to resolve adequately the high-energy region of the flow. Given this constraint, the initial three-dimensional spectra of the homogeneous high-energy region $E_H(k)$ was chosen to match the spectra measured in the Comte-Bellot & Corrsin (1971) experiment at stage 1. This experimental spectra was fitted with the following function,

$$E_H(k) = \frac{ak^4}{(k^4 + q^4)^{1+\alpha}} \exp(-bk^\beta), \tag{3.1}$$

which contains several parameters a, q, b, α and β. This fairly complicated function has been chosen because it allows an easy fit of various properties of the energy spectrum. For instance, the parameters b and β can be used for characterizing the viscous range of the spectrum. The parameters q and α determine the energy peak and the transition between the energy-containing scales and the viscous range. Finally, a determines the total energy. The function (3.1) does not allow us to derive analytical expressions for the total energy and the total dissipation in terms of the parameters a, q, b, α and β. It is thus not possible to express these parameters in terms of simple global experimental data and we have not found a systematic procedure for prescribing them. It has, however, been observed that the following set of parameters, $a = 10.6$, $q = 1.5$, $b = 0.02$, $\alpha = 1.233$, $\beta = 1.1$, allows us to fit almost perfectly the Comte-Bellot & Corrsin spectrum. Of course, the value of some of these parameters might depend on the units chosen to perform the simulation. This is not really an issue since the time scale and the length scale can be seen as entirely defined by the computational domain size $l_x = 2\pi$, $l_y = 4\pi$, $l_z = 2\pi$ and by the viscosity, chosen here to have the numerical value of 0.006. In the Veeravalli & Warhaft (1989) experiment, the ratio of energy between the two homogeneous regions is 6.27 while the ratio of dissipation is 7.28. These two ratios can be reproduced well by choosing the spectra of the low-energy homogeneous region to be of the same form as (3.1), but with the following parameters: $a = 2.74$, $q = 3.33$, $b = 0.027$, $\alpha = 1.233$, $\beta = 1.1$. Furthermore, with the above choices of parameters, the maxima of the two spectra are separated by a ratio that matches the inverse ratio of the initial integral length-scales in the Veeravalli & Warhaft (1989) experiment between the low- and high-energy regions. Accordingly, the differences in typical sizes of the large-scale structures on both sides of the mixing layer are also reproduced. From these definitions, it is possible to compute numerically the two functions $B_L(k_\perp, y)$ and $B_H(k_\perp, y)$ required in (2.6) using (2.5). The initialization procedure is then fully defined if the smoothing function $f(y)$ is prescribed. Here, the following choice has been adopted:

$$f(y) = \begin{cases} 0 & \text{if } 0 < y < 5l_y/24, \\ 1/2\left(\sin\left(12\pi\dfrac{(y - l_y/4)}{l_y}\right) + 1\right) & \text{if } 5l_y/24 < y < 7l_y/24, \\ 1 & \text{if } 7l_y/24 < y < 17l_y/24, \\ 1/2\left(\sin\left(12\pi\dfrac{(y - 2l_y/3)}{l_y}\right) + 1\right) & \text{if } 17l_y/24 < y < 19l_y/24, \\ 0 & \text{if } 19l_y/24 < y < l_y. \end{cases} \tag{3.2}$$

With this smoothing function, the high-energy region and the combined low-energy regions have the same length. Both are five times larger than each of the two

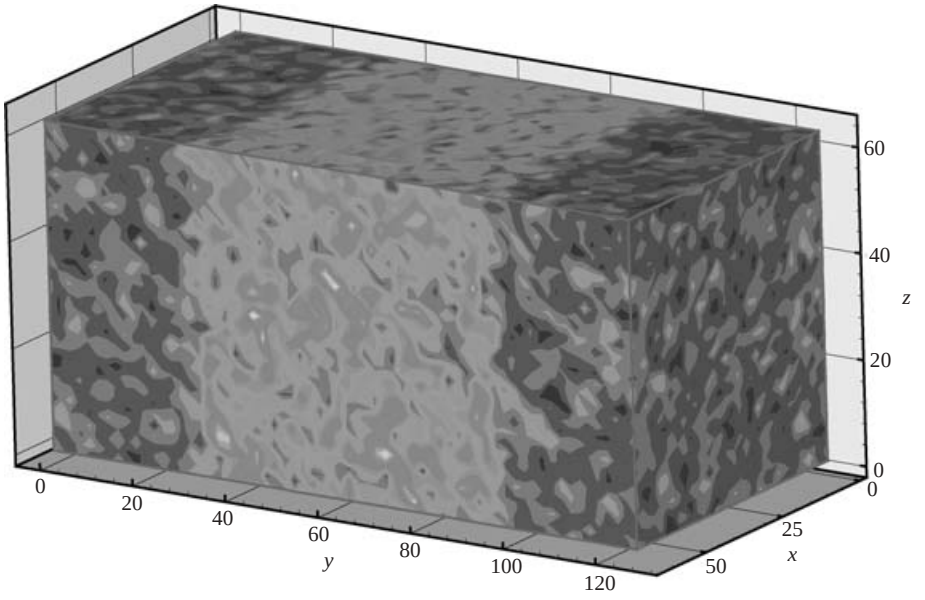

FIGURE 2. Three-dimensional contour plot of the energy density for the initial velocity field. The labels indicated on the figure correspond to grid-points. The data field was sampled every four grid-points in order to produce the graph.

mixing layers. As an illustration, the contour plot of the initial energy density is shown in figure 2. As far as the numerics are concerned, our DNS was performed using a pseudo-spectral dealiased code. The grid resolution adopted consists of $512 \times 1024 \times 512$ points. The higher-resolution dimension being the direction of inhomogeneity, taken here to be y.

3.2. *Kinetic energy diagnostics*

One of the major motivations of this study is to investigate the effect of inhomogeneities on the turbulence properties. Since the direction of inhomogeneity is along y, it is convenient to present statistics obtained by averaging over the x and z directions. For instance, the kinetic energy and dissipation rate profiles are calculated from the expressions:

$$E(y) = \tfrac{1}{2}\overline{|u_i(\boldsymbol{x})|^2} = \frac{1}{n_x n_z} \sum_{x,z} \tfrac{1}{2}|u_i(\boldsymbol{x})|^2, \tag{3.3}$$

$$\epsilon(y) = 2\nu \overline{S_{ij}(\boldsymbol{x}) S_{ij}(\boldsymbol{x})}, \tag{3.4}$$

where $S_{ij}(\boldsymbol{x}) = (\partial_i u_j + \partial_j u_i)/2$. Here, and in the rest of this paper, the overbar denotes averaging over the planes perpendicular to the direction of inhomogeneity. Figures 3(a)–3(d) represent the profiles of the kinetic energy and the dissipation rate at three different times in the simulation (both absolute and normalized profiles are plotted). Time has been normalized using the initial eddy turnover time, $t^* = t\epsilon_0/k_0$ where t is the dimensional time, k_0 is the initial average turbulent kinetic energy and ϵ_0 is the initial average dissipation rate. With the definitions (3.3–3.4), the average energy density is given by $E = n_y^{-1} \sum_y E(y)$ and a balance equation can be derived by multiplying the Navier–Stokes equation by the velocity before taking the average

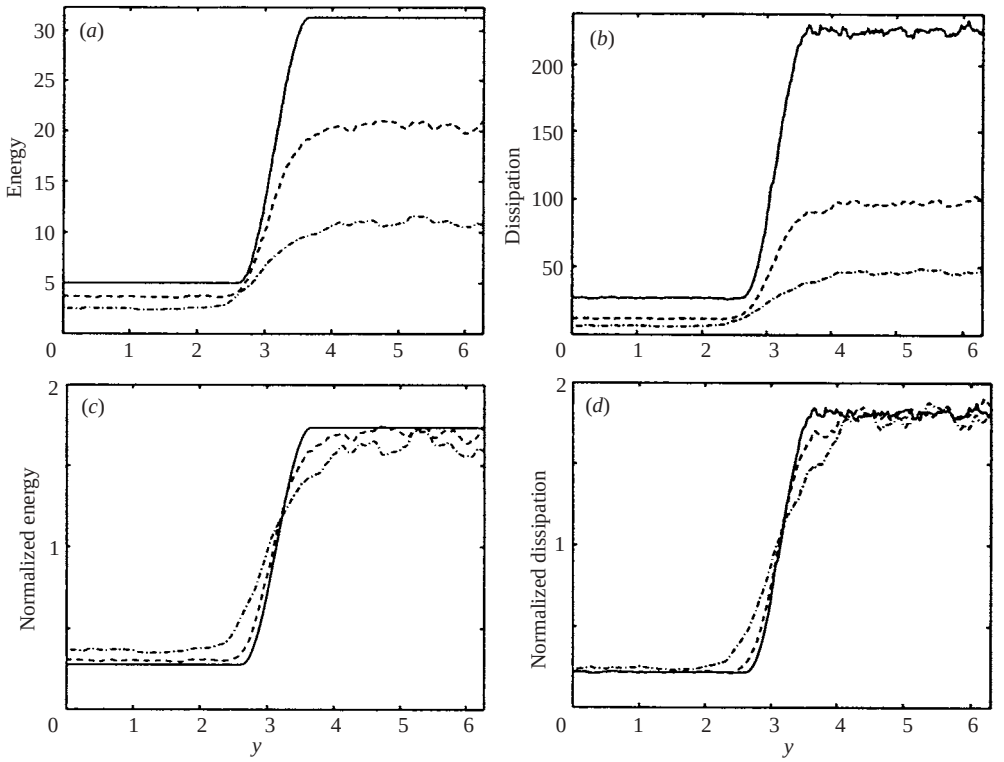

FIGURE 3. (*a*) Energy and (*b*) dissipation rate profiles across the mixing layer calculated from (3.3) and (3.4); (*c*) energy and (*b*) dissipation rate profiles normalized by their average value at the times considered; ——, $t^* = 0$; ---, 0.56; – · –, 1.51.

over the plane x, z:

$$\partial_t E(y) = -\partial_y \Phi(y) - \epsilon(y). \tag{3.5}$$

The plane-averaged energy thus evolves owing to two types of terms. The first one is the derivative of a flux which does not affect the total energy, but modifies its spatial distribution in y. It is the sum of three terms corresponding, respectively, to a convective flux $\Phi^c(y) = \overline{|u_i|^2 u_y/2}$, a pressure flux $\Phi^p(y) = \overline{p u_y}$ and a viscous flux $\Phi^v(y) = \overline{2\nu S_{iy} u_i}$. Although we do not report here graphs with the detailed contributions of each term to the total flux, it is systematically observed that, at the Reynolds number of the present simulation, $\Phi^v(y)$ is by far the smallest contribution to the total flux. Because it appears in divergence form, the flux term does not contribute to the total energy balance. As shown in figure 4, the flux contribution appears to have no mean component inside the homogeneous layers. In the mixing layer, however, the situation is different and the flux term is systematically negative and corresponds to a positive contribution to the local energy balance. As a result, the flux term almost cancels the viscous dissipation and tends to maintain a higher energy level in the mixing layer.

Figure 3 shows that as the decay proceeds, the mixing layer widens but the homogeneous regions remain largely discernible. A measure of the energy decay would be the ratio between the energy profile and its time derivative $E(y,t)/\dot{E}(y,t)$. This would provide a direct and instantaneous estimate of the characteristic decay time as a function of the position y. However, such a profile appears to be highly

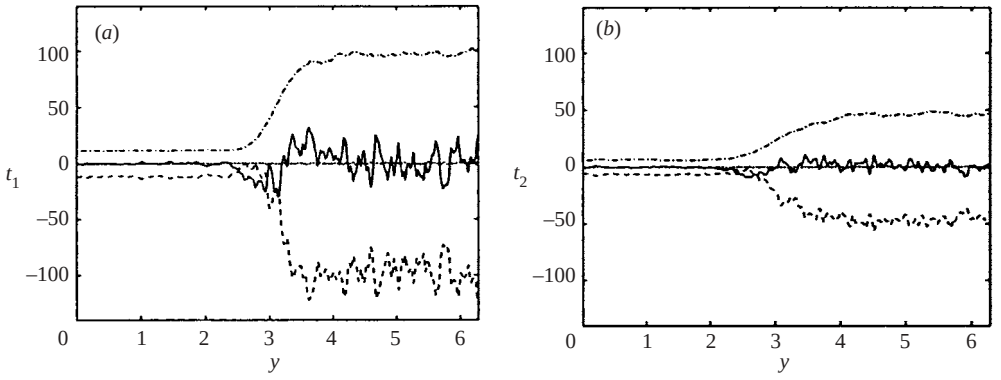

FIGURE 4. Profile of the terms entering the plane-average energy balance at (a) time $t^* = 0.56$ and (b) 1.51. $-\cdot-$, dissipation $\epsilon(y)$; ———, flux $\partial_y \Phi(y)$; ---, time derivative of the plane-average energy $\partial_t E(y)$. The sum of these three terms must be zero to numerical accuracy, as shown by the dotted line.

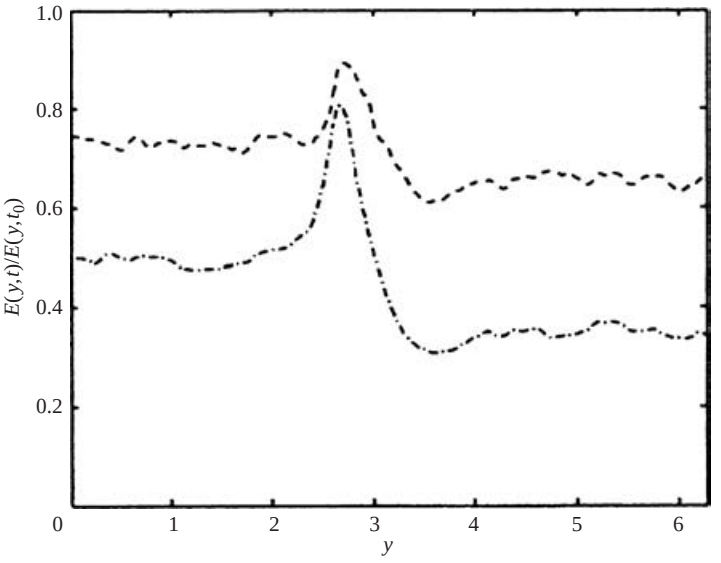

FIGURE 5. Energy profile normalized by initial energy profile. ---, $t^* = 0.56$; $-\cdot-$, 1.51.

fluctuating even at the resolution used in the present DNS. The main reason is that the flux contribution to the evolution of $E(y, t)$ has no definite sign despite having a non-negligible averaged amplitude. A more stable measure is given by the energy profile rescaled by its initial value $E(y, t)/E(y, 0)$. Figure 5 clearly provides two important pieces of information about the energy decay. First, it appears that the decay rate is proportionately different between the two homogeneous regions. Even though both regions correspond to nearly homogeneous and isotropic turbulence, this is not surprising since they are characterized by different Reynolds numbers and different flow structures, as highlighted in figure 2. Secondly, as expected, the energy exchanges between the two layers (predominantly from the high- to the low-energy region) are responsible for a local and well-marked peak in the rescaled energy profile corresponding to a significant drop in the decay rate in the mixing layer.

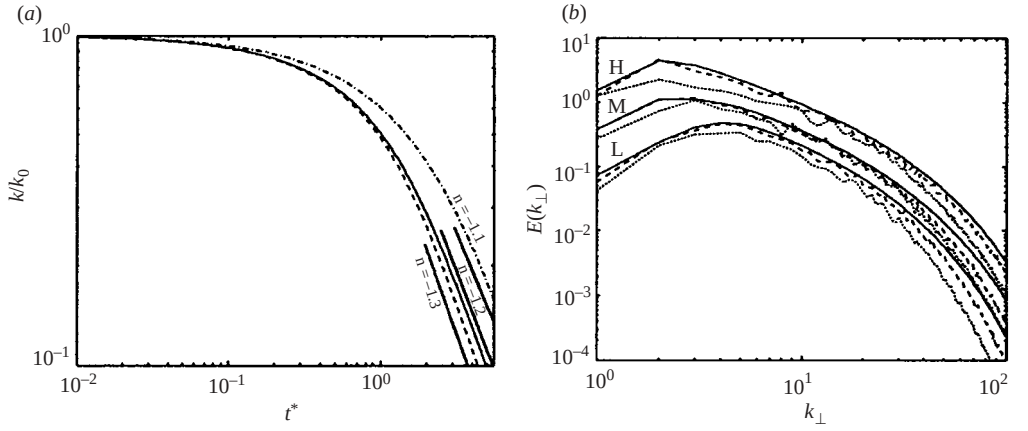

FIGURE 6. (*a*) Energy decays of the high (---) and low (– · –) energy homogeneous regions; (———) represents the global energy decay. All curves have been normalized using their initial value of k_0. (*b*) Two-dimensional spectra $E(k_\perp, y)$ (defined by (2.4)) computed inside the high (H) and low (L) homogeneous regions and the mixing-layer (M) for three different times; ———, $t^* = 0$; ---, 0.56; – · –, 1.51.

Figure 6(*a*) provides similar information and shows the temporal decay of the average energy in the high-energy and low-energy homogeneous regions. Assuming an asymptotic power-low decay $E(t) \sim t^n$, a decay exponent of $n = -1.3$ is found in the high-energy homogeneous region while in the low-energy region the decay exponent is $n = -1.1$ (the global energy decay has a decay exponent of $n = -1.3$). This difference is obviously reflected in figure 5 as the two layers have experienced a different proportional energy loss. These decay rates are compatible with the DNS of Briggs *et al.* (1996) for which a k^4 low wave-vector energy spectrum was adopted as in the present simulation. In figure 6(*b*) the two-dimensional spectra defined in (2.4) are presented to confirm that the flow is sufficiently resolved. As was observed in Briggs *et al.* (1996), the energy of the high wavenumbers decays faster with time than the energy of the low wavenumbers. It is noted that for the discretization used and the times considered, the energy peaks remain at a constant wave-vector in the homogeneous regions. The strong influence from the homogeneous layers seems to induce a shift of this energy peak in the mixing layer towards higher wave-vectors, though this effect remains moderate for the times considered.

The plane-averaged energy and dissipation profiles can be used to define a local in y microscale Reynolds number R_λ and viscous length η:

$$R_\lambda(y) = \frac{2}{3}\sqrt{\frac{15}{\nu\epsilon(y)}}E(y), \tag{3.6}$$

$$\eta(y) = \left(\frac{\nu^3}{\epsilon(y)}\right)^{1/4}. \tag{3.7}$$

Figures 7(*a*) and 7(*b*) display the distribution and evolution of these quantities. Starting from $R_\lambda \approx 30$ and $R_\lambda \approx 70$, respectively, in the low- and the high-energy layers, the Reynolds number is then observed to drop significantly in the high-energy layer while it remains approximately constant owing to the respective decay of both energy and dissipation in the low-energy layer. Figure 7(*b*) indicates that according to the criteria $k_{max}\eta \geqslant 1.5$, the flow appears to be well resolved throughout the

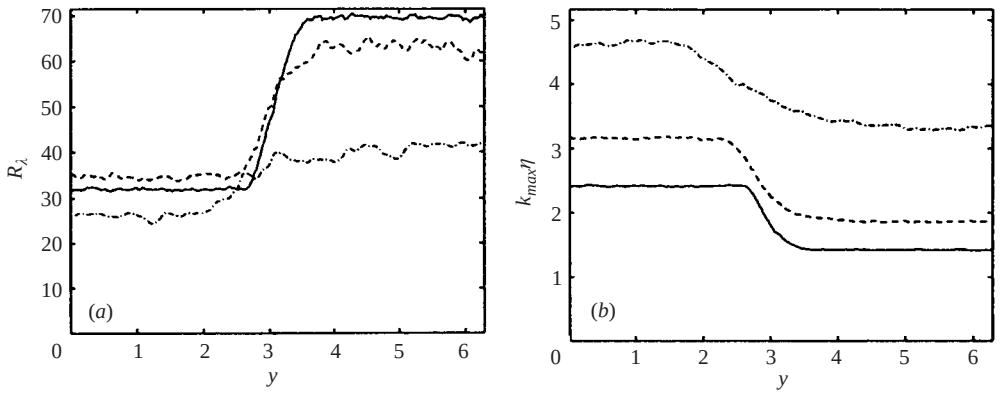

FIGURE 7. (*a*) Microscale Reynolds number profiles and (*b*) $k_{max}\eta$ profiles at three different times; ——, $t^* = 0$; ---, 0.56; – · –, 1.51.

mixing layer. In the present DNS, $k_{max} = (2\pi/l_x)(nx/2) = (2\pi/l_y)(ny/2) = (2\pi/l_x)(nz/2)$ is identical in each direction since twice as many modes are used in the y-direction than in the other directions while the computational domain is also twice as large in that direction.

3.3. *Variance profiles*

Figure 8 contains the variance profiles $\overline{u^2}$, $\overline{v^2}$ and $\overline{w^2}$ at different times as well as corresponding experimental points taken from the Veeravalli & Warhaft (1989) experiment (for the 3 : 1 perforated plate). The curves have been normalized as in Veeravalli & Warhaft (1989). First, each variance (e.g. $\overline{u^2}$) is normalized by the (average) value it reaches in the high-energy homogeneous region (e.g. $\overline{u_H^2}$). Secondly, the curves are centred around their inflection points (respectively, y_1, y_2 and y_3 for u, v and w). Finally, the direction y is normalized by the half-width $l_{1/2}$. This quantity is defined by mapping the lower and upper sides of the variance profile of u, respectively, to 0 and 1 and measuring the distance $l_{1/2}$ between the positions at which this profile reaches 0.25 and 0.75. Thus, $l_{1/2}$ is computed only from the variance profile of u, but used to normalize all three profiles. At each time presented, this normalization procedure is applied to our numerical data. The experimental points are obtained by averaging those found in Veeravalli & Warhaft (1989) for the three different distances from the grid. As was observed in Veeravalli & Warhaft (1989), the collapse of the profiles at the different times is fairly good using the above normalization and we observe that the comparison with the experiment is also satisfying. The collapse of the profiles is quite surprising at first sight since energy is expected to be transported from the high-energy to the low-energy homogeneous layer. However, the reasonable collapse observed in both the DNS and the experimental data is because the energy ratio between the two homogeneous layers varies much less than the energy levels.

The time evolution of the half-width $l_{1/2}$ of the mixing layer is compared to the integral length scales $\ell = E^{3/2}/\epsilon$ in the homogeneous layers (figure 9). The evolutions of these characteristic large-scale lengths do not seem to be correlated. During the initial stages $t \lesssim 0.7$ of the simulation, $l_{1/2}$ remains practically constant. After that, it appears to grow logarithmically.

This transition might be related to the time required for building the phase in the initially random velocity field. Indeed, the amplitudes of the Fourier modes at $t = 0$ are prescribed by the initialization procedure. However, the initial phases of

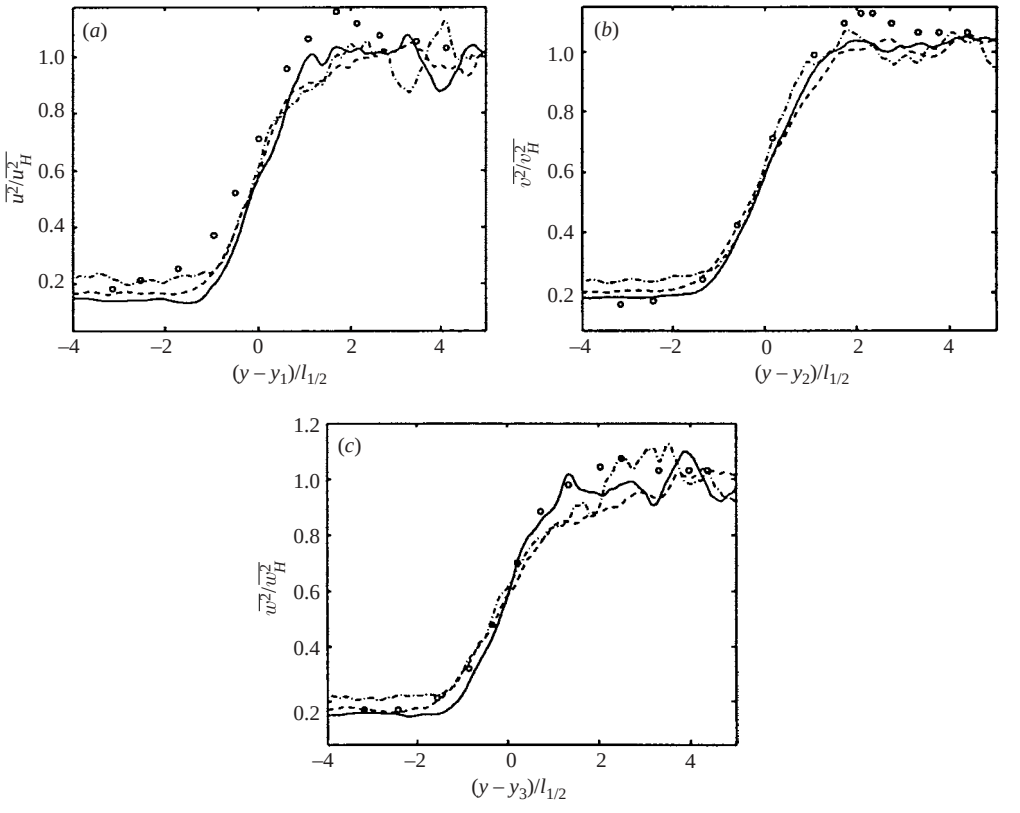

FIGURE 8. Variance profiles of the velocity components at three different times; ———, $t^* = 0$; ---, 0.56; — · —, 1.51; ○, experimental data from Veeravalli & Warhaft (1989).

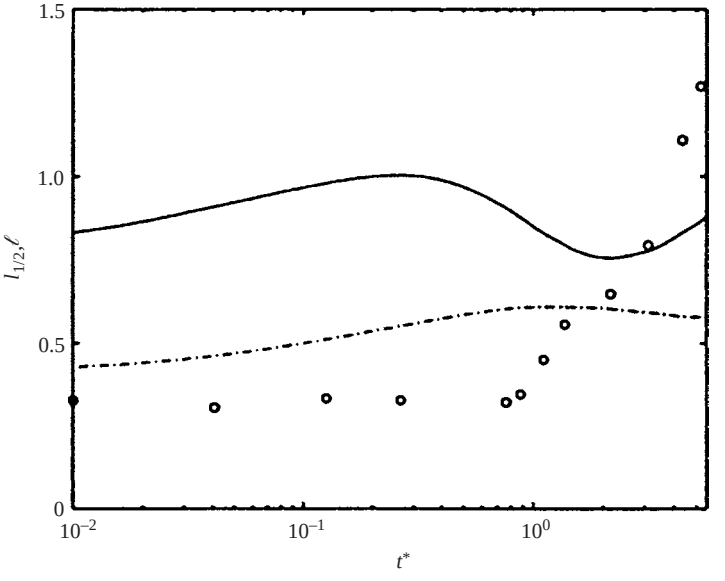

FIGURE 9. Evolution with time of the half-width $l_{1/2}$ and integral length-scales ℓ in the homogeneous layers. ○, $l_{1/2}$; ———, ℓ in the low-energy homogeneous region; – · –, ℓ in the high-energy homogeneous region.

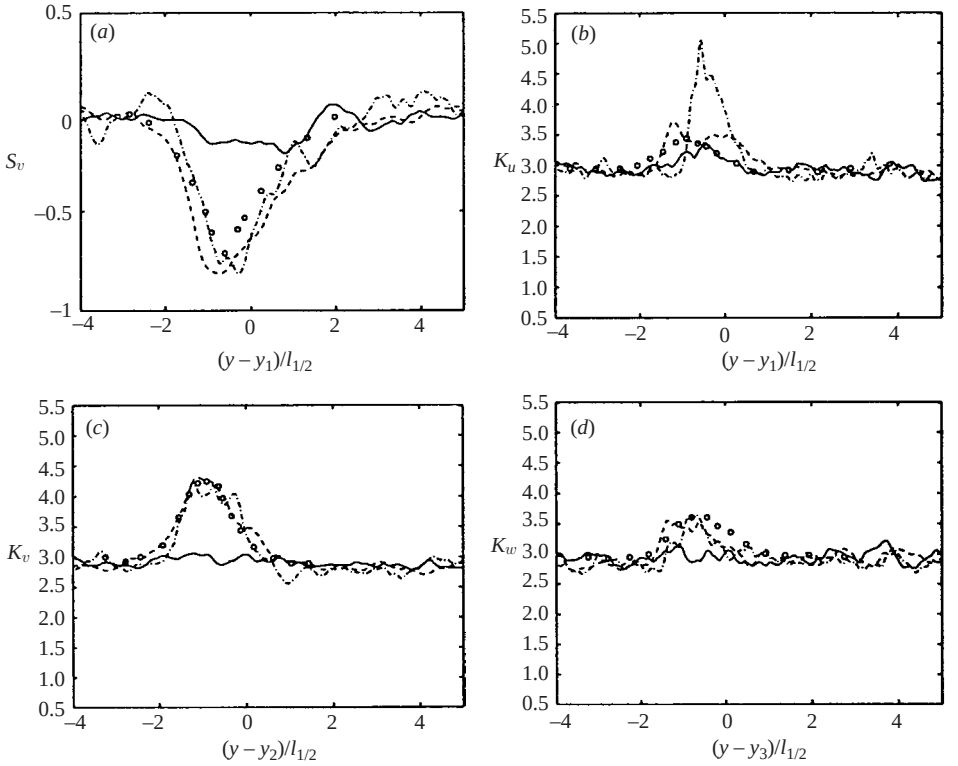

FIGURE 10. (*a*) Skewness of v; (*b*) kurtosis of u; (*c*) kurtosis of v; (*d*) kurtosis of w; ———, $t^* = 0$; ---, 0.56; – · –, 1.51; ○, experimental data from Veeravalli & Warhaft (1989). At $t^* = 0$, the numerical curves are close to their Gaussian value since the penetration mechanism described in the text has not occurred yet.

these modes are essentially random. This affects a series of quantities such as the skewness and the kurtosis that require a certain transition time before matching the experimental data. This might also explain the time required to observe an asymptotic decay for the energy (which is also of the order of $t \approx 0.7$). For the times considered, the evolutions of the integral length scales ℓ do not exhibit a transition or a clear trend.

3.4. *Intermittency*

The skewness and kurtosis of a velocity component u_i are, respectively, defined as,

$$S_{u_i} = \frac{\overline{u_i^3}}{\left(\overline{u_i^2}\right)^{3/2}}, \quad K_{u_i} = \frac{\overline{u_i^4}}{\left(\overline{u_i^2}\right)^2}. \tag{3.8}$$

For homogeneous isotropic turbulence, measures of these quantities show that they are very close to those calculated for a Gaussian signal, i.e. $S = 0$ and $K = 3$.

The skewness profile of v is shown in figure 10(*a*). The y-direction has been normalized as in figure 8 for the variance profiles. The skewness profile of v exhibits a sharp deviation from the Gaussian value around the location of the mixing layer. As described in Veeravalli & Warhaft (1989), this behaviour is attributed to the intermittent penetration into the low-energy region of structures originating from the high-energy region (a similar penetration of structures from the low-energy region

into the high-energy region is certainly also happening, but is, however, much less frequent). Agreement with experimental data from Veeravalli & Warhaft (1989) is very good, both in terms of the location of the peak and its amplitude. For symmetry reasons, it is expected that the skewness of u and w should remain close to zero. Up to statistical deviations, this is confirmed in our simulation (although not illustrated in this paper).

Kurtosis profiles of the velocity components are shown in figure 10(*b–d*) and display deviations from the Gaussian value of 3 again around the location of the mixing layer. In the Kurtosis of u, we observe an unexpectedly high peak in the profile (compared to the experimental data). At this point, we attribute this to the profile being computed from a single realization of the flow (although averaging in the (x, z)-planes was performed). We also note, however, an initial small peak in this Kurtosis component present in the initial condition (in contrast to the Kurtosis of the other two velocity components), but it is not clear whether or not it was amplified during the evolution of the flow and by what mechanism. The other two Kurtosis profiles agree very well with the experimental data again both in terms of the location of the peaks and their amplitudes.

Both the numerical simulation and the experiments indicate that the deviations from the Gaussian values for S and K occur on the low-energy side of the inflection points. This supports the idea that these deviations result from the more likely penetration of intermittent structures from the high-energy region into the low-energy region. Finally, it must be stressed that the initialization procedure presented in § 2, though quite sophisticated, does not allow imposition of the initial skewness or the kurtosis profiles in the region of the mixing layer (Gaussian values are, in fact, observed everywhere for the initial profiles as shown in figure 10 except for a small deviation for K_u, as mentioned above). The fact that the DNS later reproduces the experimental profiles observed in the mixing layer indicate that the transport mechanisms are successfully resolved.

3.5. *Anisotropy*

Briggs *et al.* (1996) observed that the shear-free mixing layer was only mildly anisotropic. Our measurements confirm this property. This is particularly important for performing LES of this flow. Indeed, most of the subgrid-scale models implicitly assume that the small unresolved scales are statistically isotropic. This is definitively the case for all the eddy-viscosity models. We have thus focused our attention on the possible anisotropy that could develop at small scales and have recorded the average square value of the velocity gradient components:

$$G_{ij} = \overline{(\partial_i u_j)^2} \quad \text{(no summation)}. \tag{3.9}$$

According to the theory of isotropic turbulence (Batchelor 1953), the following relation should hold for all $i \neq j$ (this property is only valid in a Cartesian coordinate system and it should be stressed that, despite the notation, G_{ij} is not a tensor):

$$G_{ij} = \tfrac{1}{2} G_{ij} \quad \text{(no summation)}. \tag{3.10}$$

Moreover, by symmetry, it is expected that G_{ii} is independent of i and that G_{ij} is independent of i and j for an isotropic turbulent flow. Based on this, the Shebalin angle (Shebalin, Matthaeus & Montgomery 1983) is also sometimes used to

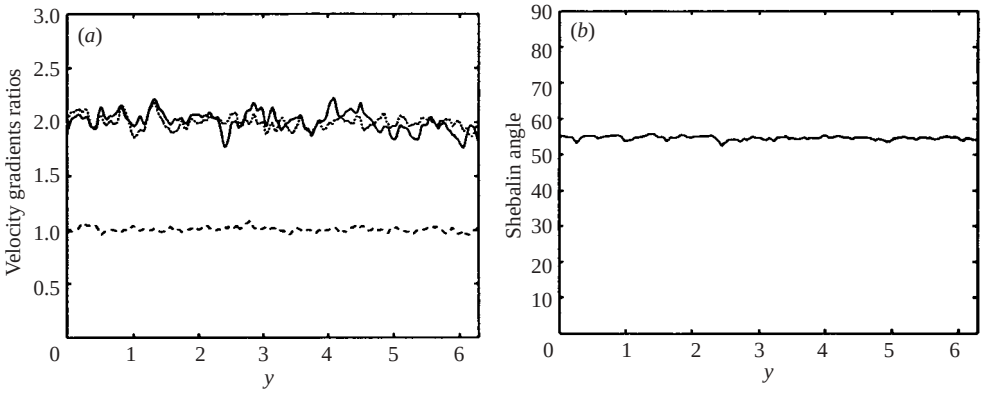

FIGURE 11. (*a*) Velocity gradients ratios as functions of y; ·····, G_{yx}/G_{xx}; ---, G_{yy}/G_{xx}; ———, G_{yz}/G_{xx}. (*b*) Shebalin angle as a function of y. All curves computed at $t^* = 1.51$.

characterize departure from isotropy for flows with one direction of inhomogeneity:

$$\tan^2\theta = 2\frac{G_{xx} + G_{xy} + G_{xz}}{G_{yx} + G_{yy} + G_{yz}}. \tag{3.11}$$

Obviously, for isotropic turbulence, $\theta = \arctan\sqrt{2} \approx 54^\circ$. As can be seen in figure 11, none of these anisotropy measures show a significant departure from isotropy. Although this is in agreement with the previous studies of the shear-free mixing layer, it is remarkable that the departure from isotropy is so weak even at the interface between the two homogeneous layers.

4. LES of the shear-free mixing-layer

4.1. *Notations and conventions – LES model*

Starting from the Navier–Stokes equations, we obtain the LES equations (4.1) by applying a filter, here denoted $\sim$ (since our code is spectral, we will only consider spectral cutoffs for the LES filter):

$$\partial_t \tilde{u}_i + \partial_j(\widetilde{\tilde{u}_j\tilde{u}_i}) = -\partial_i \tilde{p} + \nu\Delta\tilde{u}_i - \partial_j\tilde{\tau}_{ij}. \tag{4.1}$$

The unknown subgrid-scale stress (SGS) tensor $\tilde{\tau}_{ij} = \widetilde{u_i u_j} - \widetilde{\tilde{u}_i\tilde{u}_j}$ must be modelled in terms of $\tilde{u}_i$ in order to close (4.1). In this work, we will use for τ_{ij} a model proposed in Wong & Lilly (1994) and further studied in Carati, Jansen & Lund (1995) and in Dantinne *et al.* (1998). This model, which can be considered as a variant of the dynamic Smagorinsky model (see Smagorinsky 1963; Germano *et al.* 1991; Lilly 1992; Germano 1992), has been shown to perform very well in the context of homogeneous isotropic turbulence and its predictions are extremely close to the dynamic Smagorinski model. The advantage of this model rests upon the ease with which its dynamic version can be implemented. The definition of the model is:

$$\tilde{\tau}_{ij} - \tfrac{1}{3}\tilde{\tau}_{kk}\delta_{ij} = -2C\tilde{\Delta}^{4/3}\tilde{S}_{ij}, \tag{4.2}$$

where $\tilde{S}_{ij} = (\partial_i\tilde{u}_j + \partial_j\tilde{u}_i)/2$ is the resolved strain tensor and $\tilde{\Delta}$ is the LES filter width. The dimensional parameter C is evaluated by introducing a second (coarser) filter $\widehat{\ }$

(the test filter) and using the dynamic procedure:

$$C = \frac{1}{2\left(\tilde{\Delta}^{4/3} - \hat{\Delta}^{4/3}\right)} \times \frac{\langle \hat{L}_{ij}\hat{S}_{ij}\rangle}{\langle \hat{S}_{ij}\hat{S}_{ij}\rangle}, \tag{4.3}$$

where $\hat{L}_{ij} = \widehat{\tilde{u}_i\tilde{u}_j} - \widehat{\hat{u}_i\hat{u}_j}$ is the Leonard tensor (note that we have systematically used the property $\widehat{\tilde{\ldots}} \equiv \widehat{\ldots}$ valid for spectral cutoffs). As in the dynamic Smagorinski model, the only free parameter available is the ratio of the spectral cutoffs: $\tilde{\Delta} / \hat{\Delta}$. In the following discussion, this ratio will be assumed to be equal to 2. For homogeneous isotropic turbulence, the averages $\langle \cdots \rangle$ in (4.3) are obtained by averaging over the whole computational domain. The idea is of course that, since turbulence is homogeneous, the constant C should be statistically independent of the position. For inhomogeneous flows in one direction, like the shear-free mixing layer or the channel flow, dependence on the direction of inhomogeneity is introduced by averaging quantities only over the other two homogeneous directions. This is justified only if the flow is not too inhomogeneous. The dynamic coefficient C then depends explicitly on the inhomogeneous direction: $C = C(y)$. Our LES condition was obtained by filtering (with a sharp spectral cutoff) the initial DNS field down to $32 \times 64 \times 32$ modes. Thus, only $1/16$ of the gridpoints are retained in each direction for the LES, meaning that there is one LES grid point for about 4000 DNS grid points. The box-size is unchanged and remains $2\pi \times 4\pi \times 2\pi$. In our study, we have also included a run obtained at LES resolution, but with no subgrid-scale stress model to emphasize the effect of the model in the LES simulation. For comparison, we have filtered the DNS fields stored during the simulation down to $32 \times 64 \times 32$ modes.

4.2. *Comparison of the filtered DNS and the LES*

Figure 12(*a*) represents the temporal evolution of the normalized global kinetic energy E / E_0. From the graph, it is clear that the simulation with the LES model reproduces this diagnostic well, whereas the run with no model does not. Likewise, figures 12(*b*) and 12(*c*) show that the two-dimensional spectra with LES modelling are in good agreement with the DNS data. Two-dimensional spectra gathered from the run with no model exhibit a strong pile up of energy in the high wavenumber side of spectra, indicating that the flow is not adequately resolved in that case.

To further illustrate the decay of the kinetic energy, we display in figures 13(*a*) and 13(*b*) the profiles of the kinetic energy at two different times. This is, of course, a more sensitive diagnostic since it retains information about the inhomogeneity of the flow. Both figures again reveal a good agreement between the DNS and LES runs and a poor behaviour of the run without modelling. Variance profiles of u, v and w have been examined (not shown) and again the LES matches the DNS very nicely, whereas the no-model simulation performs poorly. For our assessment of LES, we have retained the same intermittency diagnostics described earlier: the skewness and the kurtosis of the velocity components. A sample of those quantities is displayed in figure 14. Once again, the LES run produces results which compare well with the filtered DNS data. Surprising at first, the run without the subgrid-scale stress model is also performing quite well. However, since the intermittency is attributed to large-scale structures penetrating the low-energy region from the high-energy region this is to be expected. Indeed, looking at the spectra displayed in figure 12(*c*), we see that the run without the subgrid-scale stress model is not ill-behaved for modes at the lowest wavenumbers.

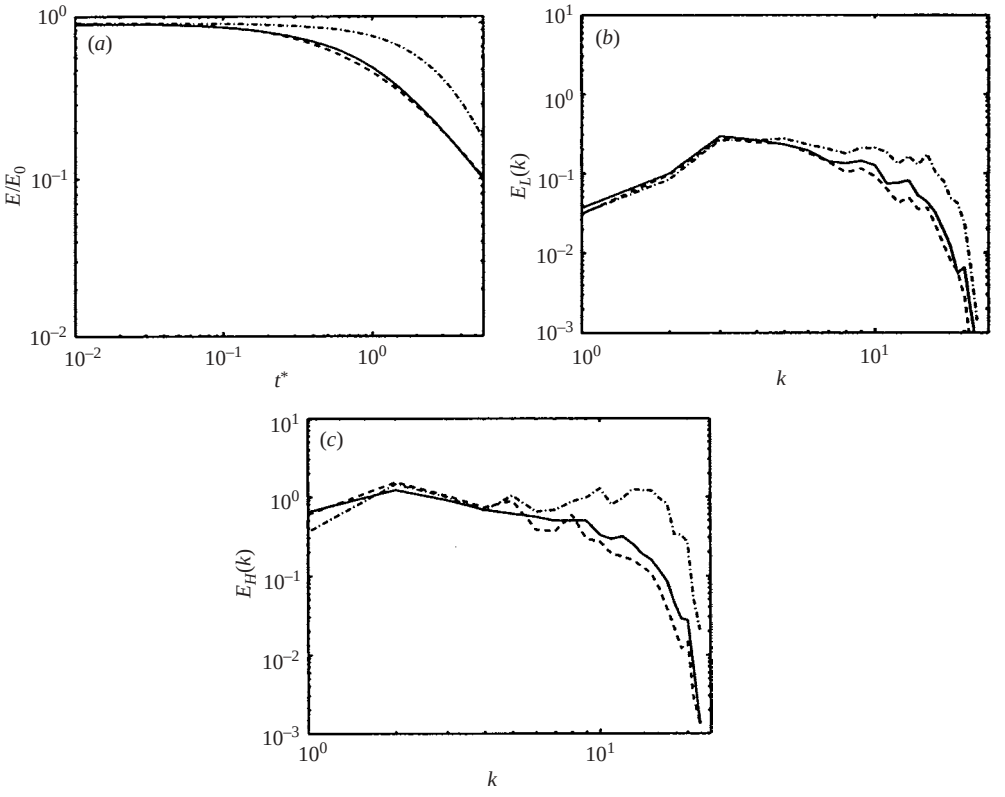

FIGURE 12. (*a*) Evolution with time of the normalized global kinetic energy E/E_0; (*b*, *c*) two-dimensional spectra $E(k_\perp, y)$ (defined by (2.4)) computed inside the high (H) and low (L) homogeneous regions for time $t^* = 1.51$. In both figures, ———, filtered DNS; ---, LES; –·–, no model.

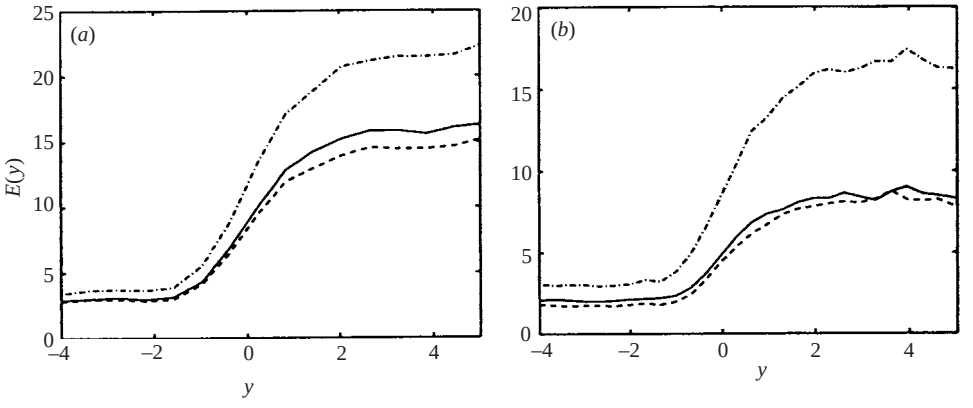

FIGURE 13. Energy profile across the mixing-layer calculated from (3.3) at times (*a*) $t^* = 0.56$; (*b*) 1.51. In both figure, ———, filtered DNS; ---, LES; –·–, no model.

4.3. *LES at infinite Reynolds number*

The preceding section seems to establish that the LES based on an isotropic eddy-viscosity model is able to reproduce satisfactorily the DNS and the experimental

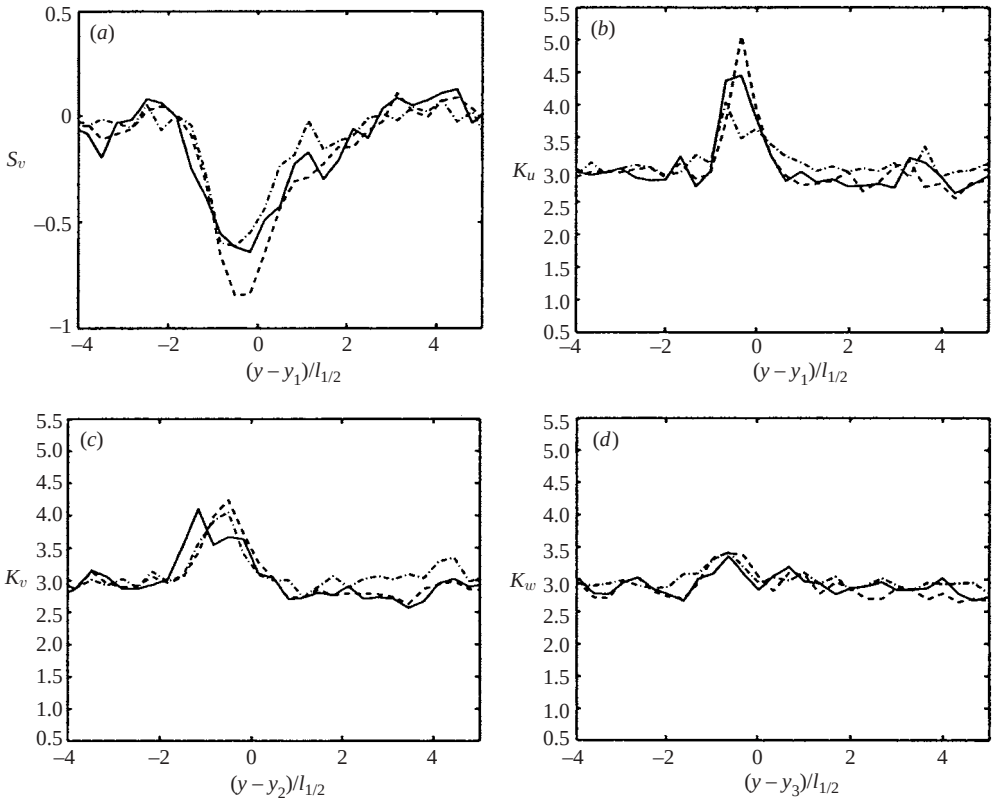

FIGURE 14. (*a*) Skewness of v; (*b*) kurtosis of u; (*c*) kurtosis of v; (*d*) kurtosis of w. All curves computed at $t^* = 1.51$. ———, filtered DNS; ---, LES; – · –, no model.

results. It is thus tempting to extend the application of the LES to Reynolds-number cases that are out of reach of DNS. In particular, we have considered the limit of 'infinite' Reynolds-number flows ($\nu = 0$), starting with the same initial condition as for the DNS, filtered down to $128 \times 256 \times 128$ Fourier modes. With the initial spectrum chosen for the DNS, such a resolution ensures that almost all the energy is captured by the LES at the beginning of the simulation. In an hypothetical DNS at $\nu = 0$, the total energy of the flow has to be conserved and energy is progressively transported from the large scales to smaller scales. In the LES, this transport mechanism has to be accounted for by the subgridscale model and the resolved energy should decrease appropriately as time passes. This, of course, means that for long times, the resolved energy in the LES only amounts to a small fraction of the total energy of the flow (as is the case in our simulation). This is somewhat contradictory with the traditional definition of an LES and indicates that the LES is pushed to an extreme limit. Nevertheless, interesting results can be extracted from this simulation.

First, it is observed in figure 15 that high-order statistics, such as the skewness and the kurtosis of the velocity distribution are very stable and close to the experimentally observed values. This confirms that these quantities depend mainly on the largest scales of the flow. Secondly, the LES with $\nu = 0$ allows us to observe the evolution of the flow for a long period without being concerned by the drop in the Reynolds number. It is thus possible to observe a longer asymptotic range in which both the energy and the subgrid-scale dissipation are following power laws. This is represented

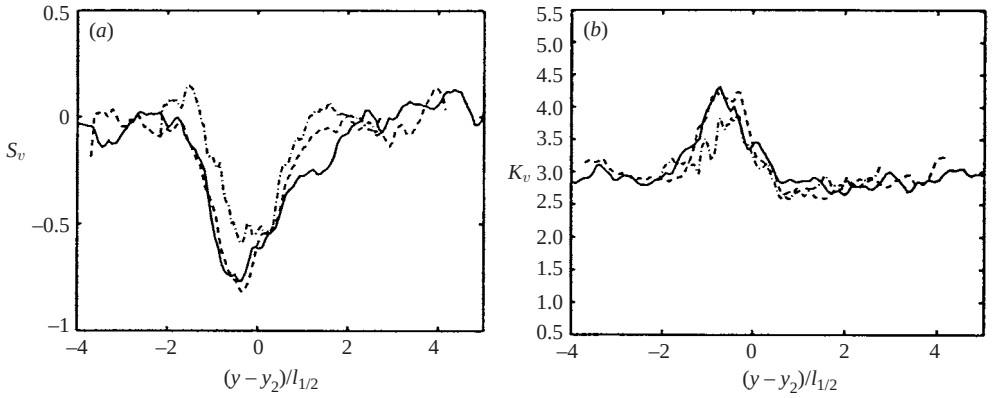

FIGURE 15. (*a*) Skewness of v; (*b*) kurtosis of v; ———, $t^* = 1.92$; ---, 3.45; – · –, 5.48; all the curves have been centred and normalized according to the procedure described in § 3.3. In particular, the width of the curves decrease with time as the half-width $l_{1/2}$ increases (see figure 17).

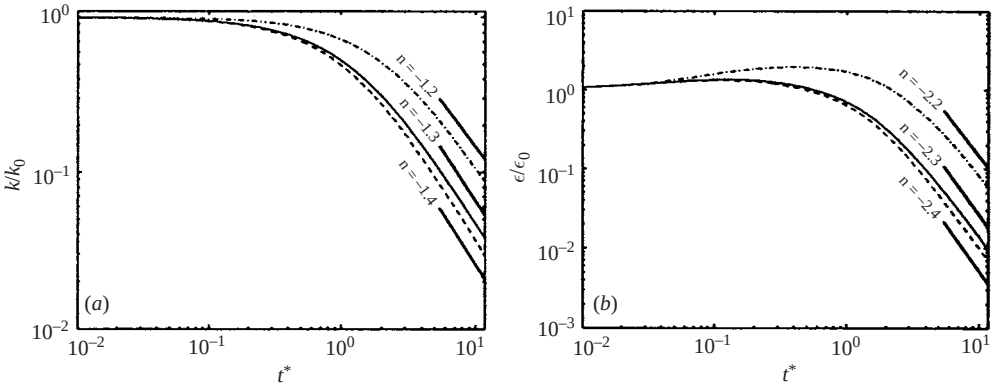

FIGURE 16. (*a*) Energy and (*b*) dissipation rate decays of the high (---) and low (– · –) energy homogeneous regions; (———) represents the corresponding global quantities.

in figure 16 and the decay exponents are reported in the figure. In this limit of infinite Reynolds numbers, the limitation in time comes from the increasing of the mixing-layer width, which, at the end of the simulation, is so large that the homogeneous layers almost disappear. The evolution of the half-width, presented in figure 17, shows the same transition as for the DNS case. Since the initial condition is essentially the same, the transition time might be due again to the building of actual turbulent phases in the Fourier modes, starting from randomly distributed phases.

5. Conclusions

This study of the shear-free mixing layer reveals that DNS is capable of reproducing most of the aspects of the experimental database that have been produced by Veeravalli & Warhaft (1989). Energy, dissipation rate and velocity variance profiles are accurately reproduced. Also, departure from Gaussianity inside the mixing layer revealed by the measurement of the skewness and the kurtosis of the velocity field are also in excellent agreement with the experimental observation. This is particularly

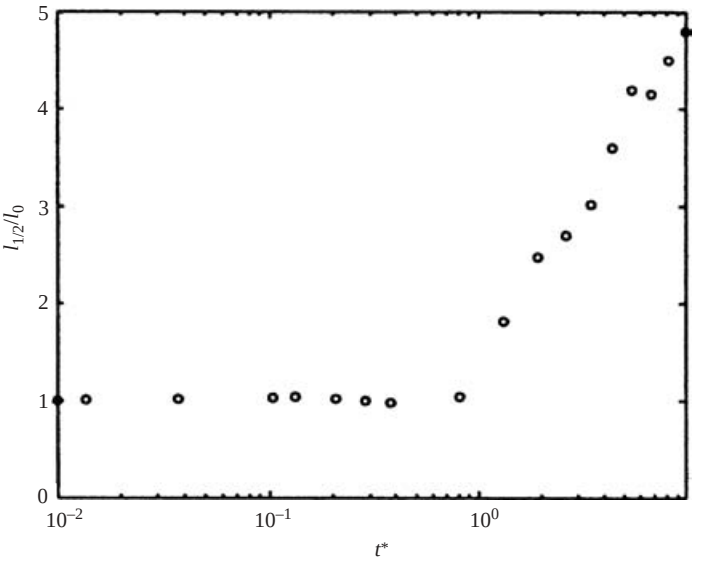

FIGURE 17. Evolution with time of the half-width $l_{1/2}$ normalized by its initial value l_0.

satisfactory since inside the mixing layer the initial values of these quantities cannot be prescribed by the initialization procedure and are entirely produced at later times by the transfer mechanisms simulated by the DNS. It is also observed that, in the absence of shear, no significant anisotropy is observed in this flow. This is consistent with previous numerical results and strongly supports the use of eddy-viscosity type models for the LES of such flows. As a consequence, it is not surprising that comparisons between the predictions of LES using such eddy-viscosity models and DNS show very good agreement. An LES in the limit of infinite Reynolds number has also been presented and the results indicate that in this limit, the major aspects of the mixing layer observed at moderate Reynolds number are retained.

The authors are very grateful to M. Rogers for his useful comments on the first version of this paper. We also thank Dr S. Veeravalli for providing data gathered during the Veeravalli & Warhaft (1989) experiment. B. K. and D. C. are researchers of the Fonds National pour la Recherche Scientifique (Belgium). O. D. is 'boursier FRIA' (Belgium). This work has been supported by the Communauté Française de Belgique (ARC 02/07-283) and by the contract of association EURATOM – Belgian state. The content of the publication is the sole responsibility of the authors and it does not necessarily represent the views of the Commission or its services.

REFERENCES

BATCHELOR, G. K. 1953 *The Theory of Homogeneous Turbulence*. Cambridge University Press.

BRIGGS, D. A., FERZIGER, J. H., KOSEFF, J. R. & MONISMITH, S. G. 1996 Entrainment in a shear-free turbulent mixing layer. *J. Fluid Mech.* **310**, 215–241.

CARATI, D., JANSEN, K. & LUND, T. 1995 A family of dynamic models for large-eddy simulation. In *Annual Research Briefs – 1995* (ed. P. Moin & W. Reynolds), pp. 35–40. Stanford University and NASA Ames Research Center: Center for Turbulence Research.

COMTE-BELLOT, G. & CORRSIN, S. 1971 Simple Eulerian time correlations of full- and narrow-band velocity signals in grid generated 'isotropic' turbulence. *J. Fluid Mech.* **48**, 273–337.

Dantinne, G., Jeanmart, H., Wickelmans, G. S., Legat, V. & Carati, D. 1998 Hyperviscosity and vorticity-based models for subgrid scale modeling. *Appl. Sci. Res.* **59**, 409–420.

Germano, M. 1992 Turbulence: the filtering approach. *J. Fluid Mech.* **238**, 325–336.

Germano, M., Piomelli, U., Moin, P. & Cabot, W. 1991 A dynamic subgrid-scale eddy-viscosity model. *Phys. Fluids* A **3**, 1760–1765.

Gilbert, B. 1980 Diffusion mixing in grid turbulence. *J. Fluid Mech.* **100**, 349–365.

Lilly, D. 1992 A proposed modification of the germano subgrid-scale closure method. *Phys. Fluids* **4**, 633–635.

Rogallo, R. 1981 Numerical experiments in homogeneous turbulence. *NASA TM* 81315. NASA, Ames Research Center.

Shebalin, J., Matthaeus, W. & Montgomery, D. 1983 Anisotropy in MHD turbulence due to a mean magnetic field. *J. Plasma Phys.* **29**, 525–547.

Smagorinsky, J. 1963 General circulation experiments with the primitive equations. *Month. Weather Rev.* **91**, 99–164.

Veeravalli, S. & Warhaft, Z. 1987 The interaction of two distinct turbulent velocity scales in the absence of mean shear. *Turbulent Shear Flows 5* pp. 31–43. Springer.

Veeravalli, S. & Warhaft, Z. 1989 The shearless turbulence mixing layer. *J. Fluid Mech.* **207**, 191–229.

Wong, V. & Lilly, D. 1994 A comparison of two subgrid closure methods for turbulent thermal convection. *Phys. Fluids* **6**, 1016–1023.